Observations of Surface Wave–Current Interaction

LEONEL ROMERO

Earth Research Institute, University of California, Santa Barbara, Santa Barbara, California

LUC LENAIN AND W. KENDALL MELVILLE

Scripps Institution of Oceanography, University of California, San Diego, La Jolla, California

(Manuscript received 30 April 2016, in final form 22 November 2016)

ABSTRACT

Wave–current interaction can result in significant inhomogeneities of the ocean surface wave field, including modulation of the spectrum, wave breaking rates, and wave statistics. This study presents novel airborne observations from two experiments: 1) the High-Resolution Air–Sea Interaction (HiRes) experiment, with measurements across an upwelling jet off the coast of Northern California, and 2) an experiment in the Gulf of Mexico with measurements of waves interacting with the Loop Current and associated eddies. The significant wave height and slope varies by up to 30% because of these interactions at both sites, whereas whitecap coverage varies by more than an order of magnitude. Whitecap coverage is well correlated with spectral moments, negatively correlated with the directional spreading, and positively correlated with the saturation. Surface wave statistics measured in the Gulf of Mexico, including wave crest heights and lengths of crests per unit surface area, show good agreement with second-order nonlinear approximations, except over a focal area. Similarly, distributions of wave heights are generally bounded by the generalized Boccotti distribution, except at focal regions where the wave height distribution reaches the Rayleigh distribution with a maximum wave height of 2.55 times the significant wave height, which is much larger than the standard classification for extreme waves. However, theoretical distributions of spatial statistics that account for second-order nonlinearities approximately bound the observed statistics of extreme wave elevations. The results are discussed in the context of improved models of breaking and related air–sea fluxes.

1. Introduction

Surface wave processes have important applications in air–sea interaction, coastal circulation, ocean remote sensing, and offshore engineering. Surface waves are important for air–sea interaction, modulating the exchange of energy, momentum, heat, and mass between the ocean and the atmosphere. Wave breaking drives upper-ocean currents and mixing (Phillips 1977), affects aerosol production (Lenain and Melville 2017), and enhances gas exchange across the air–sea interface (Thorpe 1982; Farmer et al. 1993), all of which have implications for climate change predictions (Loewen 2002).

Wave–current interaction, that is, the effects of currents on waves, include refraction due to wave propagation over spatially varying currents and wave action conservation that can result in wave steepening for waves encountering an opposing current and vice versa. Wave–current interaction modulates the ocean roughness (Phillips 1984; Munk et al. 2000) and can enhance nonlinear effects such as wave breaking, which affect satellite remote sensing products such as ocean color (Gordon 1997; Moore et al. 2000) and radar imaging (Phillips 1984; Kudryavtsev et al. 2005). Similarly, wave–current interactions can lead to the formation of extreme wave heights (White and Fornberg 1998; Onorato et al. 2011; Toffoli et al. 2015; Janssen and Herbers 2009). Wave breaking can be a good visual indicator of wave–current interactions. As shown by Melville et al. (2005), areas of enhanced wave breaking due to wave–current interaction are often associated with sea surface temperature (SST) fronts. An example of a feature studied in this paper is shown in Fig. 1 displaying a

Denotes content that is immediately available upon publication as open access.

Corresponding author e-mail: Leonel Romero, leromero@eri.ucsb.edu

DOI: 10.1175/JPO-D-16-0108.1

FIG. 1. Area of enhanced breaking due to wave–current interaction. Photo taken looking north off the coast of Bodega Bay, California, 17 Jun 2010. The black region in the lower right of the image is due to the frame of an open window of the aircraft.

photograph of the sea surface with a ''line'' of enhanced breaking due to wave–current interaction. Surface waves can also be modulated because of changes in relative wind forcing and changes in stability of the atmospheric boundary layer across mesoscale oceanic fronts with warmer water leading to intensification of the surface winds (Friehe et al. 1991; Jury 1994), which in turn modulates the surface wave field (e.g., Hwang 2005), resulting in increased wave breaking (Chelton et al. 2006). Gallet and Young (2014) recently showed that wave refraction induced by the vorticity of the Antarctic Circumpolar Current and equatorial surface current can result in significant deviations of swell from great circle paths across the Pacific Ocean. This roughly explains the outliers from the analysis by Munk et al. (1963, 2013) who, by not accounting for refraction by currents, traced swell measured off Southern California along great circle paths back to Antarctica, rather than the Southern Ocean.

Several field studies have characterized the modulation of the wave field by tidal (Vincent 1979; Masson 1996; Pearman et al. 2014) and large-scale currents (Kudryavtsev et al. 1995, Wang et al. 1994; Haus 2007). However, more measurements are needed to improve numerical wave models and wave breaking parameterizations in conditions with strong wave–current interaction (e.g., Romero and Melville 2010a; Banner and Morison 2010; Ardhuin et al. 2010, 2012). This study presents novel wave observations from two experiments over areas with significant wave–current interaction, including characterization of the modulation of the directional spectrum, wave breaking, and wave statistics. The paper is organized as follows: Section 2 introduces the environmental conditions, field experiments, and instrumentation. Section 3 describes the analysis and results, which are discussed and summarized in sections 4 and 5, respectively.

2. Field experiments

This study presents field observations from two experiments: 1) the Office of Naval Research (ONR) High-Resolution Air–Sea Interaction (HiRes) Departmental Research Initiatives (DRI) program and 2) an experiment in the northern Gulf of Mexico (GoM). Both field campaigns collected wave observations from aircraft allowing characterization of inhomogeneities of the wave field over areas with strong surface currents and current gradients. The HiRes data analyzed in this study were collected at the edge of an upwelling jet off the coast of Northern California where significant gradients of wave breaking were observed (Fig. 1). The experiment in the GoM gathered observations near the northernmost edge of the Loop Current, including an area of opposing waves and currents, and a focal region.

a. HiRes

The HiRes program was designed to study air–sea interaction processes with a focus on wave phase–resolved physical processes, such as airflow over waves including both realistic large-eddy simulations (Sullivan et al. 2014) and field observations (Grare et al. 2013). Other field measurements included broadband spectral distributions of breaking waves, from air entraining to microbreakers (Sutherland and Melville 2013), surface turbulence measurements (Sutherland and Melville 2015), and aerosols (Lenain and Melville 2017). This paper presents airborne wave observations over areas with significant wave–current interaction collected near Bodega Bay on 17 June 2010 during upwelling conditions with 13 m s^{-1} winds toward the southeast (SE). A composite map of SST from the Moderate Resolution Imaging Spectroradiometer (MODIS) in Fig. 2a shows an upwelling front at about 50 km from the coast. Supporting surface current observations were available from an existing array of 12-MHz high-frequency (HF) radars located near Bodega Bay and Point Reyes (Kaplan et al. 2005; Kaplan and Largier 2006). A snapshot of the surface currents measured by the coastal HF radars is shown in Fig. 2b. The current map shows a strong upwelling jet, reaching maximum currents of 1 m s^{-1}, with strong horizontal shear on the eastern side where the area of enhanced breaking (Fig. 1) was observed, as shown by a solid white line. This study focuses on the modulation of the wave field across the edge of the coastal jet.

1) HIRES INSTRUMENTATION

Several platforms operated during HiRes, including the Research Platform (R/P) *Floating Instrument Platform* (*FLIP*), the Center for Interdisciplinary Remotely-Piloted

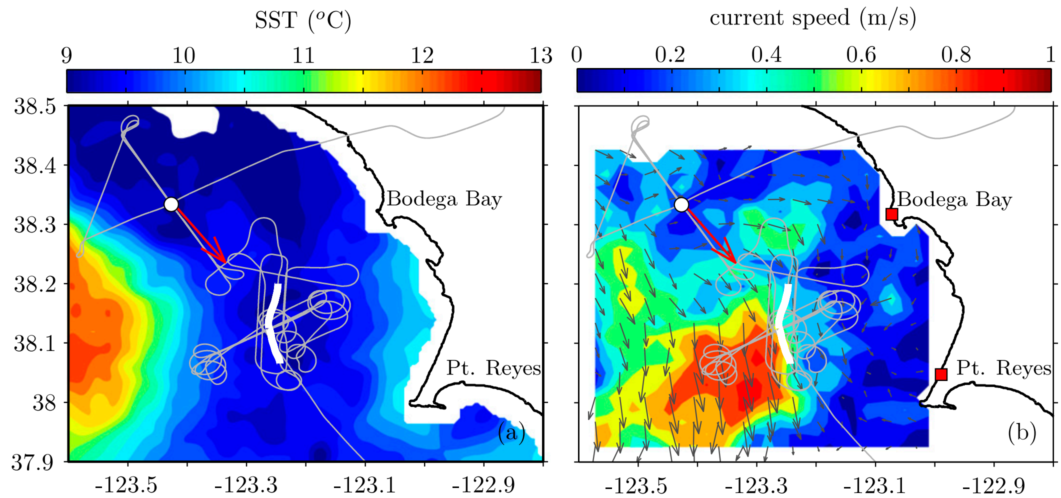

FIG. 2. (a) Composite map of sea surface temperature off Northern California from MODIS sensors onboard *Aqua* and *Terra* satellites on 17 Jun 2010. (b) HF radar surface currents with vectors decimated by a factor of 2. The gray line shows the fight track of the Twin Otter aircraft, and the thick white line indicates the area of enhanced breaking (see Fig. 1). The red arrow indicates the mean wind direction measured at FLIP (white circle). The red boxes in (b) show the location of the HF radars.

Aircraft Studies (CIRPAS) Twin Otter (TO) aircraft, R/V *Sproul*, and Aspen Helicopters' Partenavia P68-C aircraft. This study focuses on the measurements collected from the TO aircraft. The flight track is shown with gray lines in Fig. 2. The TO was equipped with two downward-looking lidars, the NASA/Edgerton, Germeshausen, and Grier (EG&G) Technical Services scanning Airborne Topographic Mapper (ATM) and a fixed Riegl (model LD90–3800EHS- FLP) nadir-looking lidar. The TO was also equipped with nadir visible and infrared (IR) imagers, a pressure sensor array in the nose cone to measure atmospheric turbulence and fluxes, a Heitronic KT19 radiometer for local SST measurement, and an aerosol measurement package. An inertial motion unit (IMU; Northrop Grumman LN100-G) with a global positioning system (GPS; Applanix POS AV 510) was used for data georeferencing. A set of two nadir-looking IMPERX IPX-11M5-L (12 bit, 4000 × 2672 pixels) synchronized cameras, each sampled at 5 Hz, were used to compute the breaking statistics described in section 3a(2). Typical spatial resolution was approximately 10–15 cm depending on flight altitude, leading to an image width in the cross-track direction ranging from 250 to 400 m and 400 to 600 m along track. Sun glitter was minimized with electromechanically controlled linear polarizers.

The ATM is a conical scanning lidar used previously to measure directional wavenumber spectra of surface waves (Hwang et al. 2000a,b; Romero and Melville 2010b). During HiRes, the ATM had a pulse repetition rate of 5 kHz, a scanning rate of 20 Hz, and a conical scanning angle of 30°. Thus, for a nominal aircraft speed of 50 m s^{-1} at an altitude $h = 300$ m above mean sea level (MSL), the theoretical horizontal resolution is $\delta x = 2.5$ m along track and $\delta y = 4.75$ m cross track, with a swath width (SW) of approximately 300 m [SW = $2h\tan(30°) \approx h$]. The calibrated elevation error per pulse is approximately 8 cm (Krabill and Martin 1987). During postprocessing the raw georeferenced ATM data were separated into forward and aft parts of the scan and then spatially binned on a regular grid with a resolution of 2.5 m; empty cells were interpolated with MATLAB's TriScatteredInterp function. Thus, the highest wavenumber resolved $k_h = 1.25$ rad m^{-1}. The lidar pulse return rate was 30% ± 3% for the forward scan and 50% ± 4% for the aft scan due to the aircraft's angle of attack (3.6° ± 0.5°). The analysis of the data was done exclusively on the aft scan with the higher pulse return rate.

2) HIRES SPECTRAL ANALYSIS

Directional wavenumber spectra were calculated from the spatially interpolated ATM data using the fast Fourier transform and the squared amplitude of the Fourier coefficients. The directional wavenumber spectrum $F(k_x, k_y)$ is defined according to

$$\langle \eta^2 \rangle = \int_{-k_h}^{k_h} \int_{-k_h}^{k_h} F(k_x, k_y)\, dk_x\, dk_y, \quad (1)$$

such that its integral over all wavenumbers corresponds to the variance of the sea surface elevation η.

Prior to calculating each spectrum, the edges of the data were tapered with a 10% Tukey window in two

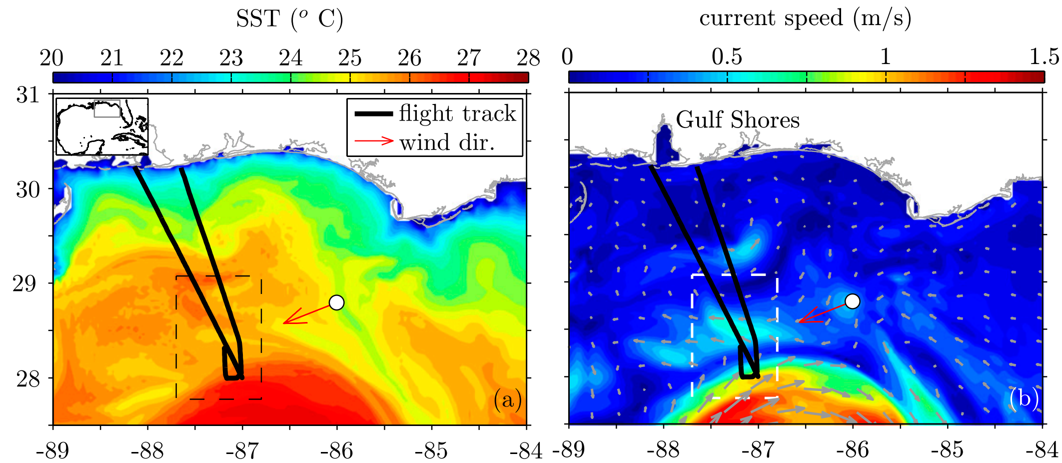

FIG. 3. (a) Sea surface temperature and (b) surface current from HYCOM reanalysis in the northern Gulf of Mexico on 30 Oct 2011. The gray line shows the coastline, the thick black line shows the flight track, and the red arrow indicates the mean wind direction from NDBC buoy 42039 (white circle). The dashed box indicates the study area. The gray arrows in (b) are the current vectors decimated by a factor of 7. The inset in (a) shows the coastline around the Gulf of Mexico and parts of the Caribbean Sea with the gray box indicating the corresponding zoomed-in area of the figures.

dimensions. Zero padding was applied in the cross-track direction; doubling the width to 600 m. Spectra were calculated from swaths 2.5 km long with 50% overlap, allowing the characterization of spatial inhomogeneities of the wave field. In addition to correcting the spectrum for the variance loss due to tapering, spectra were corrected for the Doppler shift induced by the relative motion between waves and the aircraft (Plant et al. 2005). Neighboring wavenumbers were averaged together in the along-track direction (x) yielding spectra with resolution $\Delta k_x = \Delta k_y = 2\pi/600 = 0.01\,\mathrm{rad\,m^{-1}}$. Resulting spectra were smoothed with a 3×3 top-hat filter, yielding 38 ($2 \times 300/600 \times 2500/600 \times 9$) degrees of freedom (DOF) per spectrum. Finally, spectral energy densities at angles larger than $\pm 90°$ from the wind direction were set to zero, and the remaining spectral components were multiplied by 2, preserving the variance with the oceanographic convention of energy propagating toward a given angle within the spectrum.

b. *Experiment in the Gulf of Mexico*

The experiment in the GoM was designed to collect airborne observations of surface waves interacting with the Loop Current and related eddies in October 2011. It was conducted in the northern part of the Gulf when the Loop Current boundary was located very far north, overlapping in time when cold fronts are common in the GoM. These cold fronts generally propagate from Texas into the northern Gulf during the fall and winter months (Henry 1979), giving rise to southward (northerly) winds followed by southwestward (northeasterly) winds as the fronts pass through. This allowed the possibility of investigating locally generated waves interacting with the Loop Current and eddies. This study focuses on the measurements collected on 30 October 2011, a day after the passage of a cold front, in winds of $8\,\mathrm{m\,s^{-1}}$. Figure 3a shows SST analysis from the Hybrid Coordinate Ocean Model (HYCOM) at 1/25° horizontal resolution in the northern Gulf of Mexico over the edge of the Loop Current. The corresponding surface currents are shown in Fig. 3b. The red arrow indicates the mean wind direction toward the southwest, and the dashed box shows the study area.

1) GoM INSTRUMENTATION

The research platform was the Partenavia P68-C aircraft operated by Aspen Helicopters. Figure 3 shows the flight track with a thick black line going across the edge of the Loop Current. The aircraft was equipped with the Modular Aerial Sensing System (MASS; Reineman et al. 2009; Melville et al. 2016; Clark et al. 2014) composed of a downward-looking raster-scanning lidar (Riegl LMS-Q680i), a long-wave infrared camera (QWIP FLIR SC6000), high-resolution video (JaiPulnix AB-800CL), and a hyperspectral imaging system (Specim EagleAISA). All instruments are time synchronized and georeferenced with a high-accuracy coupled GPS/IMU (Novatel SPAN-LN200). The raster lidar provides higher spatial resolution than the ATM and other airborne lidars used previously to measure ocean waves (cf. Hwang et al. 2000a; Romero and Melville 2010b; Reineman et al. 2009; Huang et al. 2012).

The raster scanning lidar has a field of view (FOV) of 60°; therefore, the swath width on the ocean surface is approximately equal to the flight altitude h. The lidar operated mainly in two modes, each setting designed to capture different scales:

Mode 1: $h = 200$ m, sampling frequency $f_s = 266$ kHz, scanning frequency $f_{sc} = 200$ Hz, and angular scan increment $\Delta\theta = 0.045°$, where $\Delta\theta = \mathrm{FOV}/M$ with $M = f_s/f_{sc}$ corresponding to the number of pulses per scan.

Mode 2: $h = 550$ m, $f_s = 60$ kHz, $f_{sc} = 70$ Hz, and $\Delta\theta = 0.07°$.

The nominal aircraft speed V_a was 50 m s^{-1}; thus, the along-track resolution for mode 1 is 25 cm (V_a/f_{sc}) and 71 cm for mode 2. The cross-track resolution at nadir is 16 and 70 cm, which increases to 20 and 84 cm at the edge of the swath for modes 1 and 2, respectively (Reineman et al. 2009). Following the method used to postprocess the ATM data, lidar data were binned and interpolated on a regular grid with horizontal resolution of 0.5 ($k_h = 6.28$ rad m^{-1}) and 1.5 m ($k_h = 2.1$ rad m^{-1}) for modes 1 and 2, respectively, before computing smoothed directional wavenumber spectra from 5-km-long swaths with 50% overlap for 75 degrees of freedom and a spectral resolution identical to that of the ATM ($dk_y = dk_x = 2\pi/600$ m $= 0.01$ rad m^{-1}).

2) GOM SPECTRAL ANALYSIS

A sample directional wavenumber spectrum from lidar measurements collected at 550 m MSL in the GoM at the edge of the Loop Current is shown in Fig. 4. The peak wavenumber $k_p = 0.08$ rad m^{-1}. The spectrum $F(k, \theta')$ is rotated such that $\theta' = \theta - \theta_w = 0°$ corresponds to the wind direction, with the wind blowing toward θ_w. The corresponding omnidirectional spectrum $\phi(k) = \int_{-\pi/2}^{\pi/2} F(k, \theta')k\, d\theta'$ is shown in Fig. 5a and is compared with a spatially overlapped spectrum measured at a lower altitude ($h = 200$ m). Both spectra agree for $k < 1$ rad m^{-1}, approximately following a $k^{-2.5}$ power law. At larger wavenumbers the spectral tail can be better approximated by a k^{-3} power law. The corresponding saturation spectra $B(k) = \phi k^3$ are shown in Fig. 5b. The directional spreading $\sigma(k)$ is defined as the root-mean-square directional width from the mean spectral direction $\overline{\theta}$ according to

$$\overline{\theta}(k) = \frac{\int_{-\pi/2}^{\pi/2} F(k, \theta')\theta'\, d\theta'}{\int_{-\pi/2}^{\pi/2} F(k, \theta')\, d\theta'},$$

and

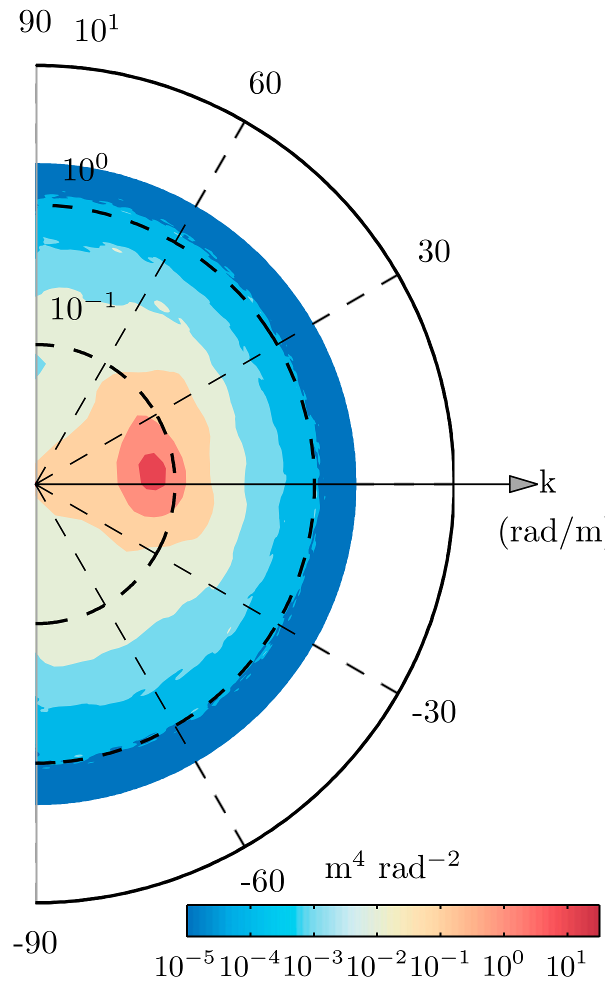

FIG. 4. Sample directional wavenumber spectrum collected at the edge of the Loop Current on 30 Oct 2011. The spectrum is rotated into the wind direction (toward 233° from true north) so the wind direction is now 0°.

$$\sigma(k) = \left\{ \frac{\int_{-\pi/2}^{\pi/2} F(k, \theta')[\theta' - \overline{\theta}(k)]^2\, d\theta'}{\int_{-\pi/2}^{\pi/2} F(k, \theta')\, d\theta'} \right\}^{1/2}. \quad (2)$$

The spreading is narrowest near the spectral peak (~15°), increasing toward both low and high wavenumbers, and approaching 55° at wavenumbers much larger than the peak (Fig. 5c). Both directional spreading curves are in good agreement except near and below the spectral peak, where the spectrum calculated from a wider swath is narrower (blue curve) and more accurate, as it is better able to resolve the directionality of the lower wavenumbers. The normalized saturation defined by $\tilde{B}(k) = B(k)/\sigma(k)$ is an important parameter for the characterization of wave breaking (Banner et al. 2002; Romero et al. 2012) and is

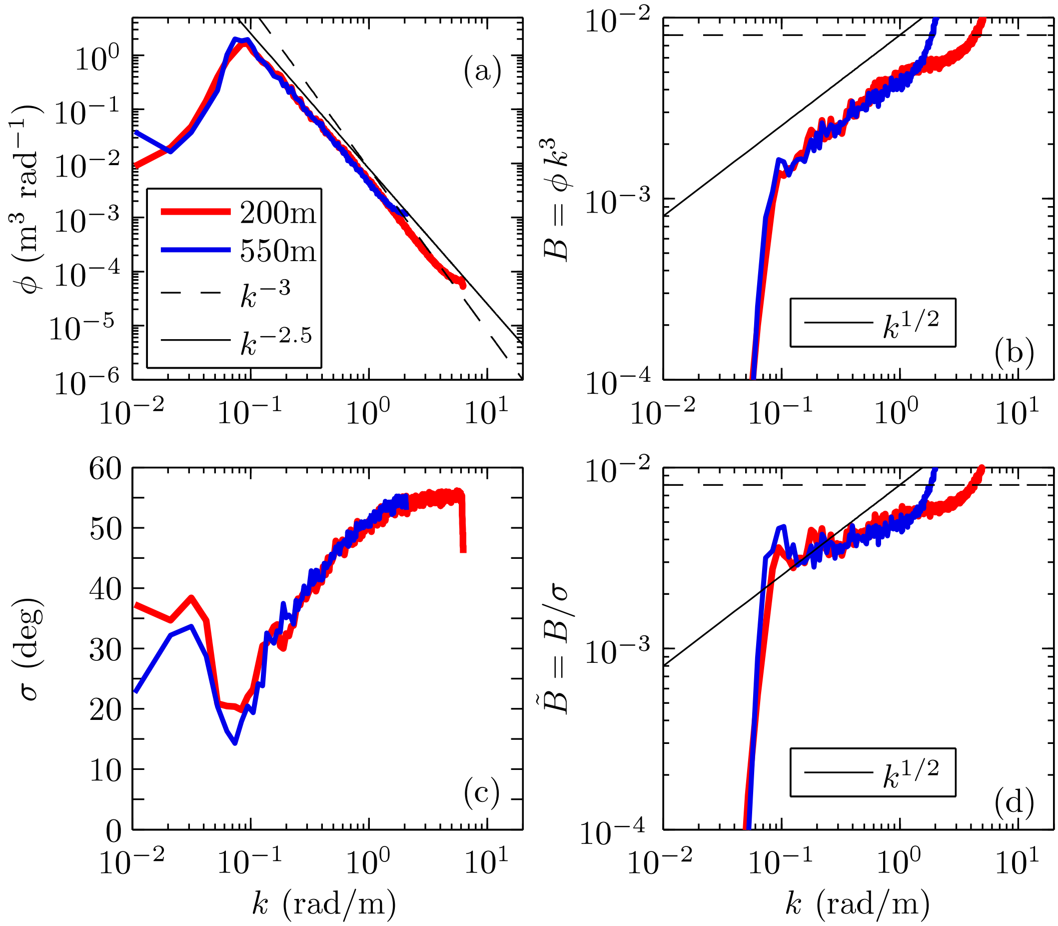

FIG. 5. Sample wavenumber spectra and their moments from lidar measurements collected at the edge of the Loop Current. (a) Azimuth integrated spectra $\phi(k)$, (b) spectral saturation $B(k) = \phi(k)k^3$, (c) directional spreading $\sigma(k)$, and (d) normalized saturation $\tilde{B} = B/\sigma$. The red and blue lines correspond to measurements collected at 200 and 550 m MSL. Note that for convenience σ in (c) is in degrees, while in (d) it is in radians. In (a) the black solid and dashed lines are reference power laws of $k^{-2.5}$ and k^{-3}, respectively.

shown in Fig. 5d.[1] When compared to the saturation spectrum, the normalized saturation exhibits a weaker increasing trend with increasing wavenumber.

3. Results

a. HiRes

During the HiRes program, on 17 June 2010, field observations were collected off Bodega Bay during upwelling conditions with steady 13 m s^{-1} winds to the southeast and waves near full development with significant wave height of 3 m. Measurements were collected over areas with strong wave–current interaction detected visually from aircraft by enhanced breaking and remote sensing of SST gradients near the edge of an upwelling jet. Figure 1 is a handheld photograph looking north, showing an area of enhanced breaking located at the edge of the jet (see also Fig. 2b). Also apparent are significant differences in the whitecap coverage on the left (west) side of the photo when compared to the right (east). A snapshot of SST measured by the IR imager on the Twin Otter is shown in Fig. 6a. The data were collected over the area of enhanced wave breaking, and it shows sharp SST gradients of about 0.4° over $O(10)$ m, corresponding to a submesoscale front partially aligned with the area of enhanced breaking. The dashed box on the bottom corresponds to the zoomed-in area of Fig. 6b, which shows frontal instabilities with horizontal scales of the order of 100 m, comparable to the wavelength of the dominant waves. The corresponding georeferenced visible imagery from the downward-looking camera is shown in Fig. 6c,

[1] Note that in Fig. 5c, the directional spreading σ is given in degrees for convenience, whereas in the normalized saturation B/σ it is given in radians.

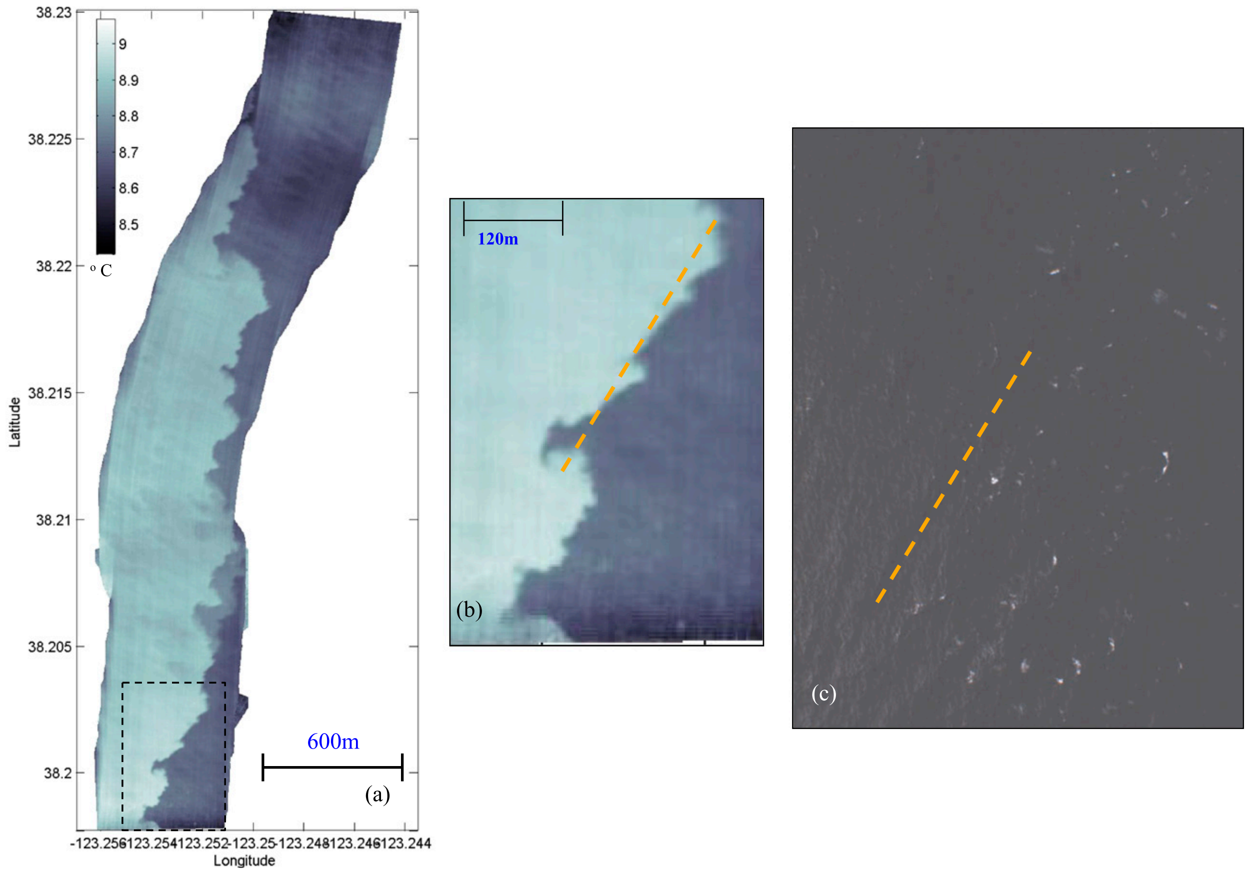

FIG. 6. (a) Georeferenced sea surface temperature map from airborne IR imagery during HiRes on 17 Jun 2010, with horizontal resolution of 2 m. The black dashed box in (a) indicates (b) the corresponding zoomed-in panel. (c) Corresponding downward-looking airborne visible image is shown. The yellow dashed line shows the approximate location of the submesoscale front in (a) and (b).

with the yellow dashed line showing the approximate location of the submesoscale front. The whitecap coverage is substantially different on each side of the front, with little or no breaking to the left (west). The photos in Figs. 1 and 6c were taken from different aircraft. The area of enhanced breaking from Fig. 1 is not evident in Fig. 6c, which only shows increased wave breaking on the lower-right corner. This is likely due to differences in dynamic range, lighting, and field of view between the downward-looking and handheld cameras. The handheld photo taken at a grazing angle covers a much larger surface area, and therefore it is easier to identify the coherent line of breaking. The position of the line of enhanced breaking was determined visually from the aircraft (white line in Figs. 2a,b) within ±1 km as it moved steadily toward the west. The line of breaking was located over an area with strong current gradients, with current speeds of 0.8 m s^{-1} to the west and decreasing down to about 0.4 m s^{-1} to the east (Fig. 2b).

A spatial cross section of the submesoscale front as measured by the Twin Otter aircraft is shown in Fig. 7a, where $x = 0$ is located within the core of the upwelling jet. The temperature drops by about 0.4° between $x = 7$ and $x = 8$ km. The vertical vorticity calculated from HF current data in Fig. 7b shows a maximum value at the edge of the temperature front. The whitecap coverage as measured from the airborne visible imagery (Fig. 7c) shows little breaking for $1 < x < 7$ km followed by increased breaking for $x > 7$ km, especially at the edge of the front. A corresponding atmospheric response can be observed in the mean winds as measured from the aircraft at 30 m MSL (Fig. 7d). The mean wind speed decreases over the segment with increased whitecap coverage to the right of the front ($7 < x < 10$ km), illustrating the coupling between the atmosphere, ocean waves, and upper-ocean currents at horizontal scales of the order of 1 km.

1) WAVE FIELD MODULATION

In contrast to single-point measurements, airborne lidar measurements allow analysis of spatial inhomogeneities of the wave field due to wave–current interactions. Here, data collected along the flight track are analyzed using

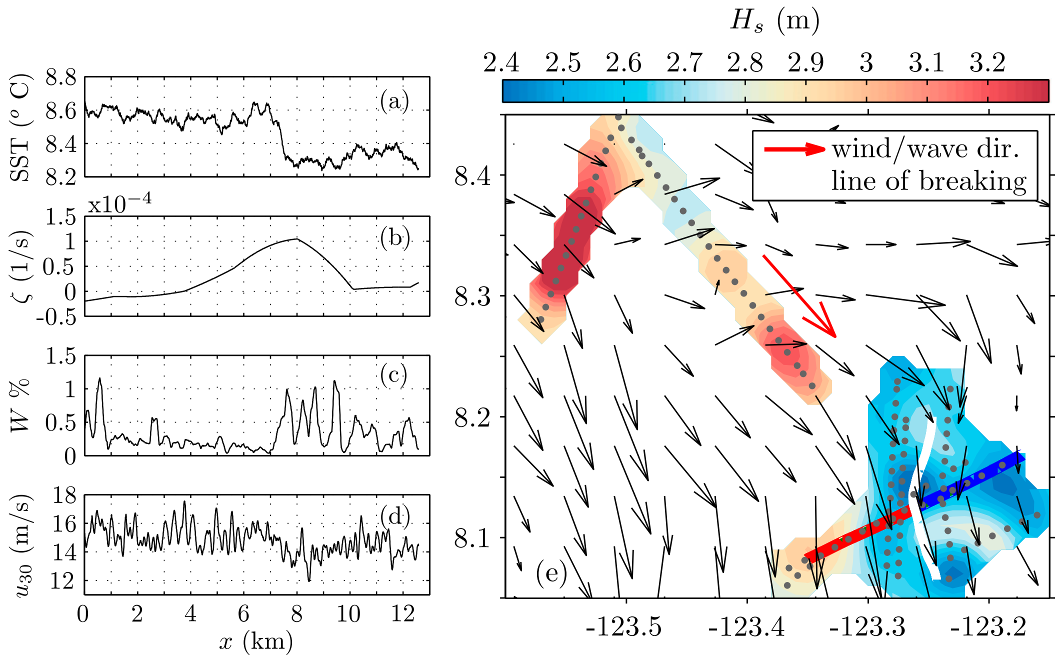

FIG. 7. Spatial cross-front distributions of (a) SST and (b) surface vorticity $\zeta = v_x - u_y$ from the HF radar surface currents at 2-km resolution; (c) whitecap coverage W and (d) wind speed at 30 m MSL measured by the Twin Otter aircraft. The position $x = 0$ corresponds to the southwest end of the sampling track in (e) shown with red and blue lines. (e) Objectively mapped significant wave height from ATM measurements, with the thick white line showing the location of the area with enhanced wave breaking (Fig. 1). The red arrow shows the mean wind and wave direction. The peak wavelength is 112 ± 12 m. The black arrows show current vectors, decimated by a factor of 2, from the HF radar data. The gray dots show the ATM sampling locations. The thick red and blue lines indicate sampling tracks with visible imagery used to process the $\Lambda(c_b)$ distributions shown in Fig. 8, corresponding to the warm and cold SST areas, respectively.

an objective analysis that maps randomly spaced data on a specified set of locations using weighted averages that depend on the spatial covariance of the data (Bretherton et al. 1976; Davis 1985). Following Denman and Freeland (1985), the structure function $G(r)$ of the significant wave height $H_s = 4\langle\eta^2\rangle^{1/2}$ was calculated from data pairs and fitted to the model $G(r) = 2V[\varepsilon + 1 - H(r)]$, where r is the distance between pairs of measurements, V is the variance, ε is the fraction of noise variance, and $H(r) = \exp(-r^2/2L^2)$ is the assumed Gaussian autocorrelation function. The fitted noise variance $\varepsilon = 0.1$ and decorrelation length $L = 2.8$ km, which is comparable to the spatial resolution of the data (2.5 km) or two adjacent data points with 50% overlap (2 × 1.25 km). Both parameters were used to calculate the objective map of H_s shown in Fig. 7e. The significant wave height H_s is on average 2.8 m, varying within 30% over the area covered by the aircraft. It is generally lower over the southeast corner of the figure, particularly to the right (east) of the jet and increases by about 8% toward the jet core, from right to left (east to west). The peak wavelength is less affected, with a mean value of 112 ± 12 m. This suggests that the modulation of the wave field across the coastal jet is mostly confined to wavenumbers larger than the spectral peak.

The airborne visible imagery collected from the downward-looking camera allowed the quantification of the spectral statistics of breaking fronts, specifically $\Lambda(c_b)dc_b$, defined as the average length of breaking crests with speed c_b in the range c_b to $c_b + dc_b$ per unit surface area (Phillips 1985). Following Kleiss and Melville (2010, 2011), $\Lambda(c_b)$ was calculated from visible imagery (ImperX IPX-11M5-L dual camera system) collected on both sides of the submesoscale front (or line of breaking), which is shown in Fig. 8 with the red and blue lines corresponding to the warm (west) and cold (east) side of the front, with sampling locations shown with red and blue lines in Fig. 7e. Each collected digital image was first georeferenced using the information from the onboard GPS/IMU and then interpolated to a regular grid with a 10-cm spatial resolution. A detailed description of the breaking statistics processing steps used in the present study is provided in Kleiss and Melville (2011). The black dashed line is a reference power law of c_b^{-6}, according to Phillips' (1985) equilibrium model. The $\Lambda(c_b)$ distributions exhibit

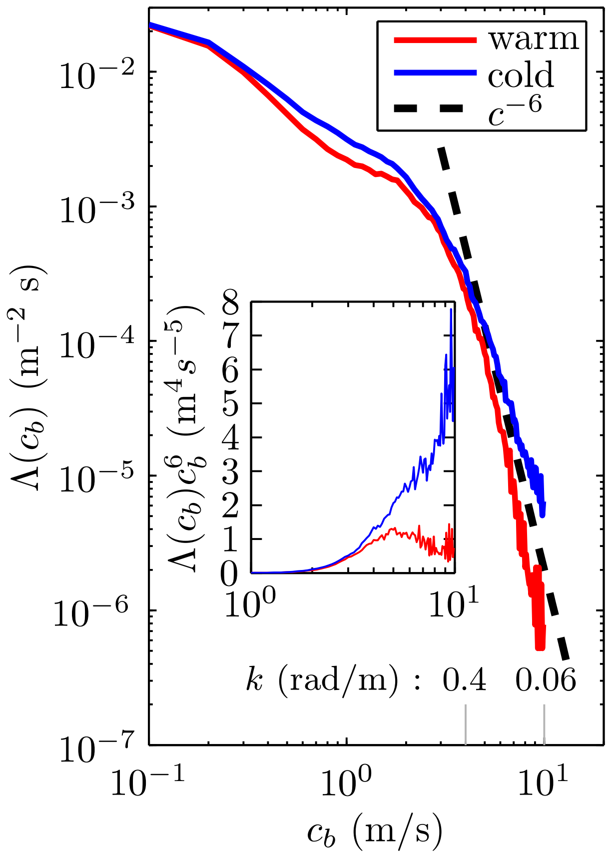

FIG. 8. Breaking distributions $\Lambda(c_b)$ across the area of enhanced wave breaking. The red and blue lines correspond to measurements over the warm and cold sides of the front, respectively. See sampling locations in Fig. 7. The black dashed line is a reference power law of c^{-6}. The two distributions exhibit the largest differences in two of the measured regions for $0.4 < c_b < 2\,\mathrm{m\,s^{-1}}$ and $3 < c_b < 10\,\mathrm{m\,s^{-1}}$ (or $1.5 < k < 40$ rad m^{-1} and $0.06 < k < 0.4$ rad m^{-1}, assuming the linear dispersion relationship and a value of $\alpha = 0.8$), with more breaking on the cold side of the front. The inset shows $\Lambda(c_b)$ compensated by c_b^6.

substantial variability, with larger values on the cold side of the front for $0.4 < c_b < 2\,\mathrm{m\,s^{-1}}$ and $4 < c_b < 10\,\mathrm{m\,s^{-1}}$. Note that for $c_b < 2$–$3\,\mathrm{m\,s^{-1}}$, the lack of air entrainment in the sampled breakers leads to a rolloff of the distribution from the c_b^{-6}, as the visible imagery cannot accurately capture the breaking fronts (Romero et al. 2012). This is consistent with Sutherland and Melville (2013), who, by using a combination of infrared and visible cameras, showed that the c_b^{-6} behavior extended to much lower values of c_b (0.1–0.8 m s^{-1}). The inset shows $\Lambda(c_b)$ compensated by c_b^6, varying by up to a factor of 5 between the warm and cold areas. The speed of the breaking front c_b is linearly related to the wave phase speed c through a proportionality factor α such that $c_b = \alpha c$, with α varying within 0.7 and 0.9 (Rapp and Melville 1990; Stansell and MacFarlane 2002; Banner and Peirson 2007; see also Banner et al. 2014; Pizzo and Melville 2016). From the linear dispersion relationship assuming $\alpha = 0.8$ (Rapp and Melville 1990), the range of breaking speeds $4 < c_b < 10\,\mathrm{m\,s^{-1}}$, where the $\Lambda(c_b)$ distributions vary the most, corresponds to wavenumbers in the range of 0.06 to 0.4 rad m^{-1} (±25%).

We further examined the spatial modulation of the directional wavenumber spectrum, focusing on the measurements around the area of enhanced wave breaking. Objective maps of mean saturation, directional spreading, and normalized saturation were calculated using the noise variance and decorrelation length obtained from the structure function of the significant wave height, as shown in Figs. 9a, 9b, and 9c, respectively. The spectral moments were averaged for $k_p \le k < 0.4$ rad m^{-1} for consistency with the range of wavenumbers where $\Lambda(c_b)$ varied the most across the front. All three parameters show substantial variability across the line of breaking when compared to H_s (Fig. 7e). The mean saturation increases, the spreading decreases, and the normalized saturation increases from left to right (west to east) across the line of breaking.

The spatial inhomogeneities of the wave field across the front are further analyzed along the sampling tracks with the available overlapping whitecap coverage W and directional wavenumber spectra. Figure 10a shows a spatial scatterplot color coded by W. There is substantial variability in W across the front, with very low values just to the left (west) of the front and relatively larger values to the right (east). The area identified as the line of enhanced breaking, partially overlapping with the submesoscale front, is apparent with large values of whitecap coverage. The corresponding mean saturation and normalized saturation averaged in the range $k_p < k < 0.4$ rad m^{-1} are shown in Figs. 10b and 10c, respectively. There is good spatial correspondence between W and $\langle B\rangle$ and the mean normalized saturation $\langle\tilde{B}\rangle$, with low values to the left (west) of the front and relatively larger values to the right (east). Correlation coefficients R between mean spectral moments and W are significant with $R = 0.64$, -0.59, and 0.80 for the saturation, directional spreading, and normalized saturation, respectively, with the normalized saturation giving the best correlation. However, the correlation difference between W and saturation $\langle B\rangle$ and the normalized saturation $\langle\tilde{B}\rangle$ is not statistically significant with a p value of 0.1 for a two-sided test. Extending the wavenumber range to $k_p < k < 1.0$ rad m^{-1} to compute the average moments, the resulting correlation coefficients are slightly reduced to $R = 0.46$, -0.43, and 0.67 for the saturation, directional spreading, and normalized saturation, respectively.

2) RAY TRACING

A ray tracing analysis was carried out following Mathiesen (1987), using the approximation that the local

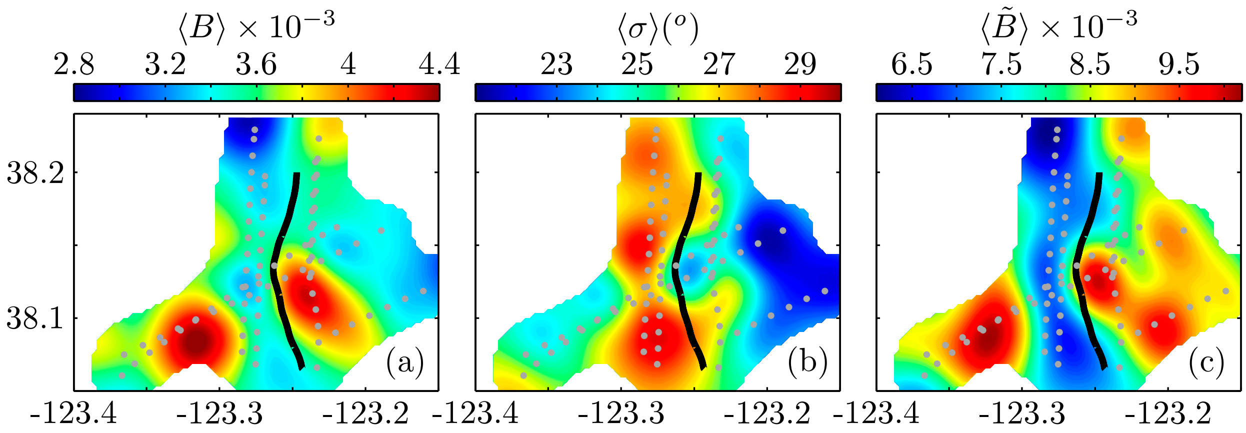

FIG. 9. Objectively mapped spectral moments across the area of enhanced wave breaking (thick black line) from lidar data. (a) Degree of saturation $\langle B \rangle$, (b) directional spreading $\langle \sigma \rangle$, and (c) normalized saturation $\langle \tilde{B} \rangle$. The brackets represent averages in the range $k_p \leq k < 0.4$ rad m^{-1}, where $k_p = 0.056$ rad m^{-1}. The gray dots indicate the mean sampling locations by the lidar.

curvature of a ray is given by the vorticity field $\zeta = v_x - u_y$ divided by the group velocity c_g (Kenyon 1971; Dysthe 2001). The ray equations were integrated using the HF radar currents and the measured mean peak wavenumber and direction. The resulting rays are shown in black in Fig. 11, plotted over the vorticity field normalized by the Coriolis parameter f. The rays are parallel or divergent immediately to the west of the front over the sampling area. On the right side of the front (east), the rays are generally convergent over the sampling area, except over the southernmost part. This is consistent with the right–left (east–west) asymmetry of the whitecap coverage (Figs. 1, 7c). It is also consistent with the wider spectrum to the left (west) and relatively narrower spectrum to the right (east) of the front (Fig. 9b). There is also ray convergence farther to the left of the line of breaking (west), where H_s and the saturation are also large: Figs. 7e and 9a, respectively. The spatial overlap between the line of enhanced breaking and the area of maximum current gradient (vorticity) suggests that enhanced breaking was likely a result of opposing waves and currents due to waves leaving the jet encountering an "opposing" current in a frame of reference relative to the jet. Repeating the ray tracing computations for wavenumbers within the range of increased values of $\Lambda(c_b)$, for example, $4k_p$, results in qualitatively similar ray patterns but with enhanced ray curvature (not shown).

b. *Experiment in the Gulf of Mexico*

In the fall of 2011, the Loop Current extended very far north in the GoM, within range of the Partenavia aircraft based at Gulf Shores, Alabama. This, combined with the high probability of offshore winds due to frequent atmospheric cold fronts during that time of the year, provided an opportunity to collect airborne measurements of waves interacting with the Loop Current (LC) and related eddies. On 30 October, the Partenavia

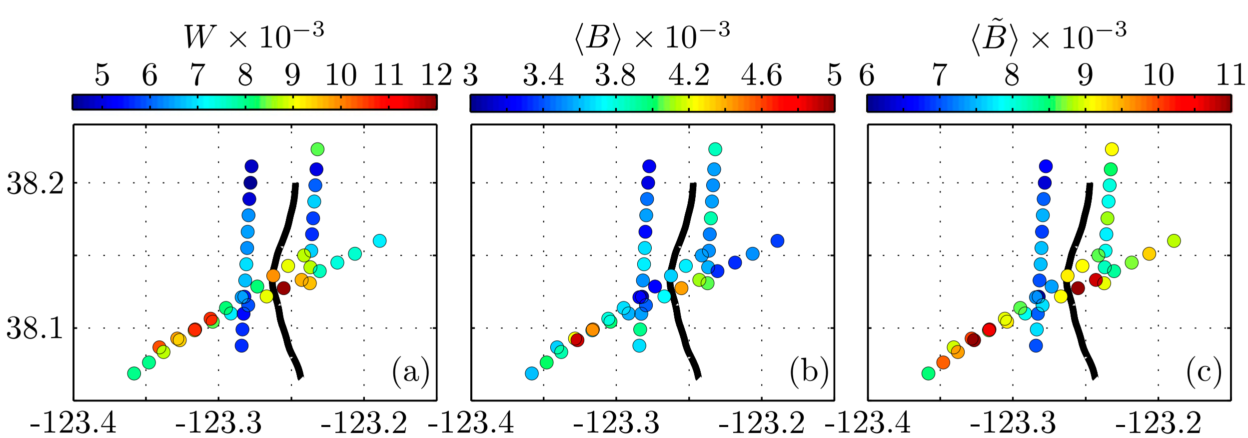

FIG. 10. (a) Fractional whitecap coverage W across the sea surface temperature front. (b),(c) Mean saturation and normalized saturation, respectively, for $k_p < k < 0.4$ rad m^{-1}. The thick black line shows the location of the area of enhanced wave breaking.

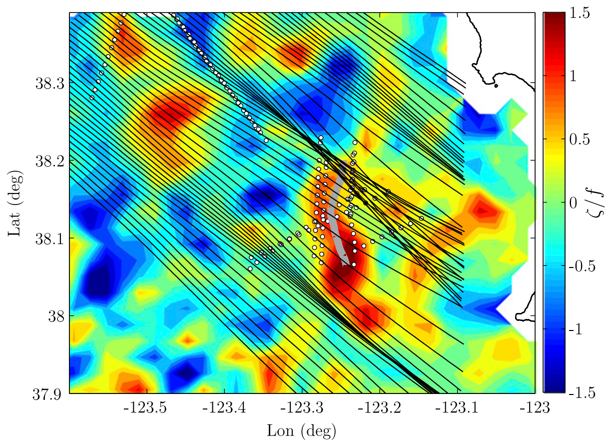

FIG. 11. Ray tracing over the surface vorticity field of the HF radar current data at 2-km resolution. The vorticity ζ is normalized by the Coriolis parameter f. Ray trajectories were integrated from the NW with mean peak wavenumber k_p and direction computed over the sampling area. The thick gray line shows the location of the area with enhanced wave breaking. The white dots show the mean sampling locations by the lidar.

aircraft collected measurements near and across the edge of the Loop Current after the passage of an atmospheric cold front.

As described above, the structure function was calculated using data pairs of significant wave height and used to fit a decorrelation length and fractional noise variance, assuming a Gaussian decorrelation function, yielding $L = 9$ km and $\varepsilon = 0.07$. These parameters were used to generate objective maps of H_s and other variables. Figure 12a shows an objective map of H_s and dominant wave direction θ_p (black arrows). The gray arrows show the surface currents from HYCOM analysis. The edge of the LC is on the lower-right corner of the figure. There is substantial variability of the dominant waves, with H_s varying by as much as 30% (between 1.3 and 1.8 m) and θ_p varying by up to 45°. The dominant waves propagate to the west at the top of the figure and toward the southwest near the LC edge. There are three maxima in H_s: one over the area of opposing waves and currents, the second to the north over a region of current convergence with collinear waves and currents, and the third in the northwest corner. The objective map of significant wave slope $\eta_{\rm rms}k_p$, defined as the product of peak wavenumber times the root-mean-square surface elevation $\eta_{\rm rms} = \langle\eta^2\rangle^{1/2}$ shown in Fig. 12b, has a distribution similar to H_s but with values consistently larger over the area of opposing waves and currents in the LC. The whitecap coverage W in Fig. 12c only shows two maxima: one maximum in the LC and the second on the northeast (NE) corner adjacent to an area of large H_s.

Objective maps of mean saturation, spreading, and normalized saturation are shown in Figs. 12d, 12e, and 12f, respectively. All three parameters were averaged for $k_p < k < 1$ rad m^{-1}, with the upper limit just before the noise floor of the spectra measured at the higher altitude (see Fig. 5). The saturation is large over the area of opposing waves and currents, consistent with the significant slope, but exhibits another maximum on the northernmost part of the mapping area. The directional spreading varies by up to 8°, showing an east–west asymmetry. The variability of the mean normalized saturation is qualitatively similar to the mean saturation but shows better correspondence with W. The correlations between W and $\langle B\rangle$, $\langle\sigma\rangle$, and $\langle\tilde{B}\rangle$ along the flight track give R = 0.45, −0.34, and 0.54, respectively, with $\langle\tilde{B}\rangle$ giving the best correlation, consistent with the HiRes observations, but again the correlation difference between $\langle\tilde{B}\rangle$ and $\langle B\rangle$ against W is not statistically significant.

1) WAVE STATISTICS

Here we first investigate the modulation of statistical distributions of wave heights, crests, troughs, and crest length due to wave–current interaction. The results are compared with analytical models including linear and nonlinear approximations. For this analysis the wave data were divided into three subsets: S1, S2, and S3, which are shown in Fig. 12b delineated with dashed black lines. The groups where chosen based on similarities of significant slope with nearby wave observations. S1, S2, and S3 contain 25, 55, and 26 data swaths, with mean significant slope $\eta_{\rm rms}k_p = 0.032 \pm 0.003$, 0.028 ± 0.003, and 0.036 ± 0.005, respectively. S3 has the largest average wave slope and S2 the lowest, consistent with Fig. 12b.

Individual crest and trough heights were calculated from each data swath along parallel lines in the direction of the dominant waves. Crests and troughs heights were calculated from the maximum and minimum elevation, respectively, between successive upward zero crossings. Individual wave heights were determined from the difference between crest and trough heights. Probability density functions (pdfs) of crest heights η_c, magnitude of trough heights $|\eta_t|$, and wave heights H normalized by the root-mean-square of surface elevation $\eta_{\rm rms}$ were calculated for each data swath. Then, pdfs from multiple swaths were ensemble averaged within each data group (S1–S3). The exceedance probability of $\eta_c/\eta_{\rm rms}$ and $|\eta_t|/\eta_{\rm rms}$ are shown in Figs. 13a and 13b, respectively. The subsets S1, S2, and S3 are shown with red, green, and blue lines, respectively, with horizontal bars corresponding to the uncertainty due to standard error of $\eta_{\rm rms}$, defined as $2{\rm std}/\sqrt{N}$, where std is the standard deviation and N is the number of samples within each data subset.

The wave crest distributions are bounded by the nonlinear Tayfun distribution with parametric dependence on the significant slope (Tayfun 1980; Toffoli et al. 2008),

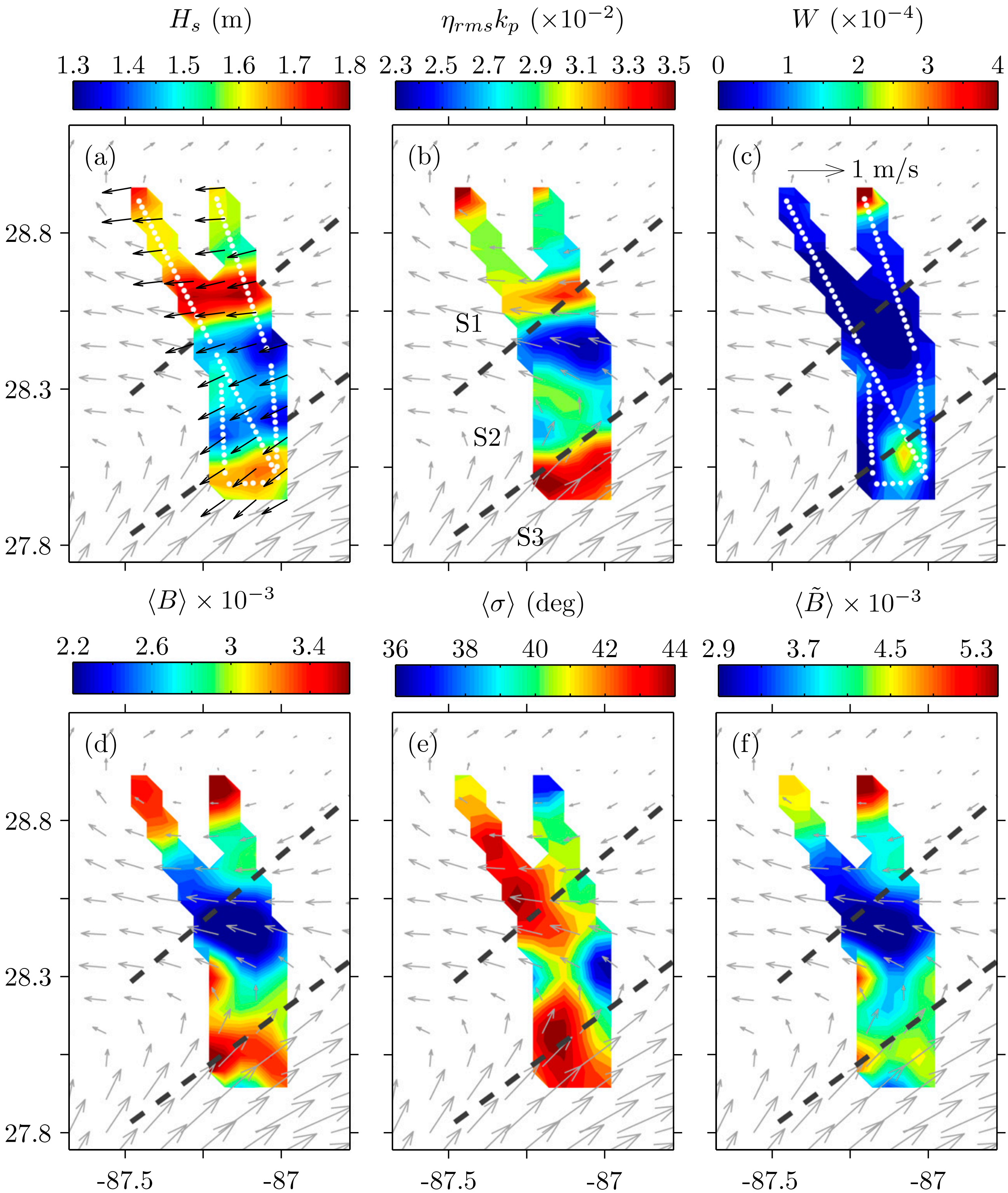

FIG. 12. Objective maps of (a) significant wave height H_s, (b) significant slope $\eta_{\mathrm{rms}}k_p$, (c) fractional whitecap coverage W, (d) degree of saturation $\langle B \rangle$, (e) directional spreading $\langle \sigma \rangle$, and (f) normalized saturation $\langle \tilde{B} \rangle$, with the brackets corresponding to a spectral average for $k_p < k < 1.0\ \mathrm{rad\ m^{-1}}$. The black arrows in (a) show the dominant wave direction and the white dots in (a) and (c) show the mean sampling locations. The gray vectors show surface currents from HYCOM analysis decimated by a factor of 2. The dashed black lines delineate the three data groups S1, S2, and S3 used to compute the wave statistics (Fig. 13).

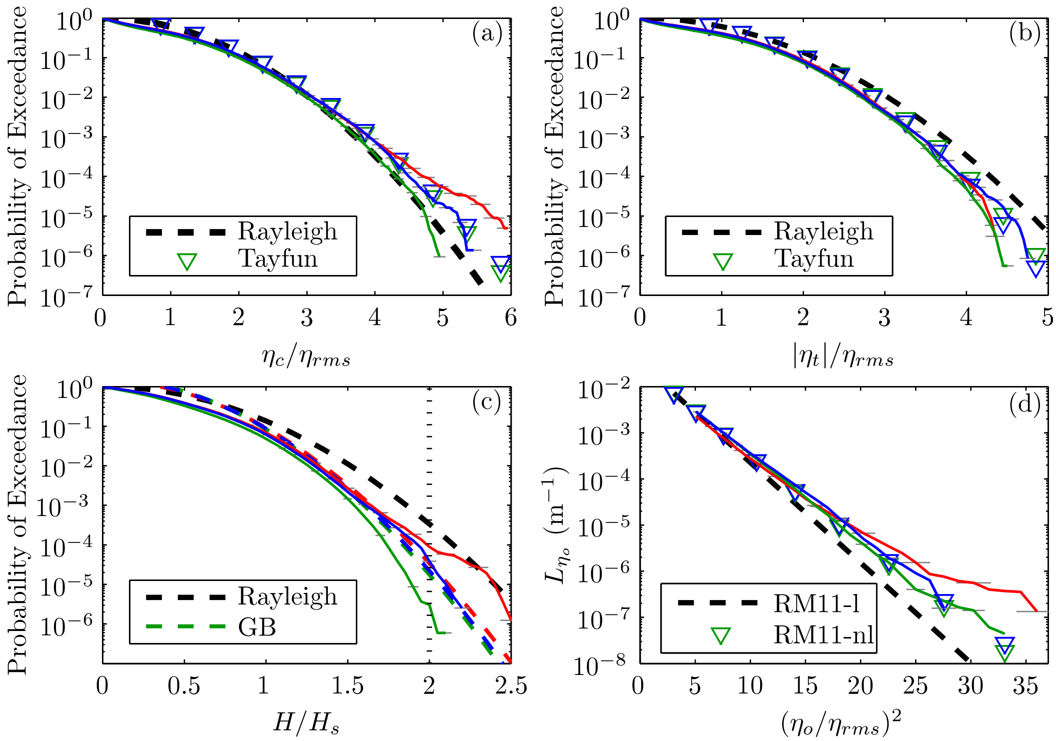

FIG. 13. Measured statistical distributions from the data subsets S1, S2, and S3, corresponding to the red, green, and blue lines, respectively. Exceedance probability distributions of (a) wave crests η_c and (b) troughs $|\eta_t|$ normalized by the root-mean-square surface elevation η_{rms} are shown. The triangles in (a) and (b) correspond to second-order Tayfun distributions with parametric dependence on the significant slope. (c) The exceedance probability of wave height H normalized by the significant wave height H_s. The colored dashed lines correspond to the generalized Boccotti (GB) distribution (Alkhalidi and Tayfun 2013). The black dotted vertical line shows the threshold criterion for extreme waves. (d) The statistical distribution of the length of crests per unit area with elevation exceeding normalized thresholds η_o/η_{rms}. The black dotted line and colored triangles correspond to the narrowband linear and second-order nonlinear distributions, respectively (Romero and Melville 2011). The horizontal gray bars correspond to the uncertainty based on the standard error of η_{rms}.

except for S1, where significant deviations from second-order theory can be observed. The wave trough distributions are generally lower than the Rayleigh distribution, in good agreement with Tayfun's distribution. The exceedance probability of wave heights H, normalized by the significant wave height $H_s = 4\eta_{rms}$, is shown in Fig. 13c and compared to the generalized Boccotti (GB) distribution, which includes effects due to finite spectral bandwidth and third-order nonlinear corrections (Alkhalidi and Tayfun 2013). The GB distribution was calculated using the spatial, two-dimensional autocorrelation function (Romero and Melville 2011) and the fourth-order cumulants of the sea surface elevation. It generally bounds the lidar measurements, except for S1 approaching the Rayleigh distribution with the maximum wave height approaching $2.55H_s$. This is much larger than the typical threshold for an extreme wave of $2H_s$.

Following the work by Romero and Melville (2011), the statistics of crest lengths were analyzed by defining $L\eta_o$ as the length of crests per unit surface area exceeding elevation threshold η_o. For this analysis the three-dimensional lidar data were thresholded at several values of positive surface displacement and then binarized. The binary images were then used to determine the length and orientation of each thresholded crest by fitting an ellipse. This allows us to calculate $L\eta_o$ and compare it against analytical distributions, including both linear and second-order nonlinear approximations, derived by Romero and Melville (2011) based on the statistical analysis of a random moving surface by Longuet-Higgins (1957). Figure 13d shows ensemble averages of $L\eta_o$ plotted against $(\eta_o/\eta_{rms})^2$. The measured distributions are well approximated by the nonlinear distribution by Romero and Melville (2011) shown with triangles, except for S1, which shows significant deviations from the second-order nonlinear distribution for large wave elevations.

The analytical distributions of wave crests, troughs, and heights shown in Figs. 13a–c are based on single-point models. However, extreme wave statistics at a point differ substantially from spatial and spatiotemporal statistics, with the latter giving the largest expected waves as the total number of waves increases (Dysthe et al. 2008; Fedele 2012). Recent studies have shown that the theoretical models of space–time statistics of extreme waves that account for second-order nonlinearities are consistent with spatiotemporal measurements collected in the Mediterranean Sea (Fedele et al. 2013; Benetazzo et al. 2015). The modeling study by Barbariol et al. (2015) suggests that space–time distributions of extreme wave heights normalized by $\eta_{\rm rms}$ increase only slightly by a few percent over areas of opposing currents due to the modulation of the spectrum by currents. Here, we compare our measurement of the extreme wave elevations against theoretical distributions of spatial extremes.

Following Fedele et al. 2013 and Benetazzo et al. 2015, the exceedance probability of wave extremes for the directional spectrum of random linear waves over a given area can be approximated by

$$P(\eta_{\rm max}/\eta_{\rm rms} > \tilde{\eta}) \approx 1 - [1 - \tilde{\eta}\exp(-x\tilde{\eta}/2)]^{N_s}, \quad (3)$$

where $\eta_{\rm max}$ is defined as the maximum surface elevation $\{\max[\eta(x)]\}$ within a spatial ensemble with N_s number of waves,[2] which is proportional to the sampling area divided by the product of the mean wavelength times the mean crest length (see appendix). Accounting for second-order bound harmonics, the nonlinear surface elevation

$$\hat{\eta} = \tilde{\eta} + \frac{\mu\tilde{\eta}^2}{2} \rightarrow \tilde{\eta} = \frac{-1 + \sqrt{1 + 2\mu\hat{\eta}}}{\mu}, \quad (4)$$

where μ is a measure of the wave steepness accounting for a correction due to spectral bandwidth (also defined in the appendix). The probability of extreme surface elevations for nonlinear waves can be directly obtained from Eqs. (3) and (4). The total number of waves N_s estimated for each data subset S1–S3 are 2.9×10^4, 5.9×10^4, and 3.0×10^4, with mean steepness $\mu = 0.045 \pm 0.002$, 0.044 ± 0.007, and 0.047 ± 0.006, respectively.

The exceedance probabilities of extreme surface elevations were calculated from all 5-km-long data records within each subset (S1–S3). The measured distributions are shown in Fig. 14 with red, green, and blue symbols corresponding to S1–S3, respectively. The corresponding linear and nonlinear theoretical distributions calculated from the average moments of the directional spectrum are shown with dashed and solid lines, respectively. The data generally exceed the linear model but are approximately bounded by the nonlinear distributions, even in S1 (within error bars), where the largest waves are found. This suggests that theoretical distributions of second-order, nonlinear, space–time statistics of extreme waves are suitable for engineering applications even in conditions with strong wave–current interactions. However, the analytical model cannot explain the relative differences in observed extreme wave heights between the different data subsets (S1–S3).

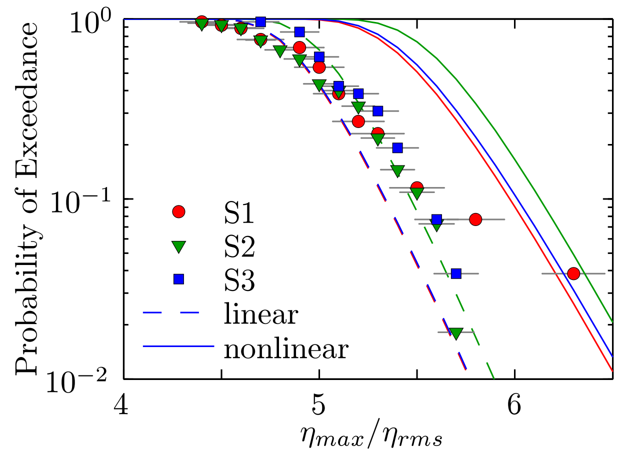

FIG. 14. Probability of exceedance of dimensionless extreme wave elevations $\eta_{\rm max}/\eta_{\rm rms}$. The circles, triangles, and squares correspond to data subsets S1, S2, and S3, respectively. The corresponding linear and nonlinear distributions of wave extremes over an area (Fedele et al. 2013) are shown with dashed and solid lines, respectively. The error bars are calculated from the error of the mean of $\eta_{\rm rms}$ due to spatial inhomogeneities.

2) RAY TRACING

A ray tracing analysis was carried out using the observed mean peak wavenumber and direction computed over the sampled area and HYCOM surface current data. Figure 15 shows the resulting rays plotted over the vorticity field normalized by the Coriolis parameter. The white dots show the location of the wave measurements from the aircraft, and the gray lines show the delineation between the different subsets (S1–S3). The rays show significant divergence over S2 where observed wave height was low (Fig. 12a). In contrast, the rays converge over S1, where H_s is largest. Also, the focal area corresponds to the data subset where the normalized maximum wave heights H/H_s and extreme elevations $\eta_{\rm max}/\eta_{\rm rms}$ are largest.

4. Discussion

The data from both the HiRes experiment off the coast of Northern California and the experiment in the Gulf of Mexico showed substantial inhomogeneities of

[2] Equation (3) does not include an additional term due to the number of the waves along the perimeter of the sampling area because it is negligible for relatively large areas.

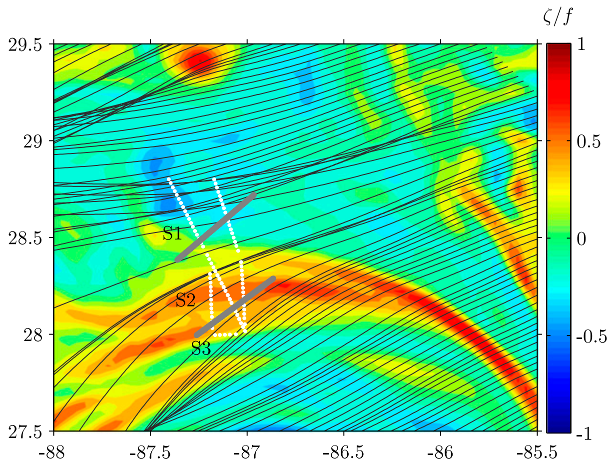

FIG. 15. Ray tracing over the surface vorticity field of HYCOM 4-km surface current data in the northern Gulf of Mexico. The vertical vorticity $\zeta = v_x - u_y$ is normalized by the Coriolis parameter f. Ray trajectories (black lines) were integrated with measured mean peak wavenumber k_p and direction and assumed constant from the NE. The white dots show the location of the airborne wave measurements. The solid gray lines delineate the three data groups (S1–S3) used to compute the wave statistics (Figs. 13 and 14).

the wave field due to wave–current interactions. In the context of wave breaking, wave–current interaction can have important implications for mixing and gas exchange between the ocean and the atmosphere. For example, the HiRes measurements showed enhanced wave breaking on the colder side of the submesoscale front. In the context of frontal dynamics, secondary circulation results in surface convergence at fronts (McWilliams 2016). This suggests that gas exchange may be enhanced not just due to enhanced wave breaking alone but also due to secondary ageostrophic circulation efficiently entraining bubbles down into the water column. Moreover, secondary circulation at fronts depends on vertical mixing (McWilliams et al. 2015), which can in turn be modulated by wave–current interactions asymmetrically across fronts.

Other possible important feedbacks include spatial gradients of the surface momentum flux due to modulation of wave breaking by wave–current interactions and vortex forces due to shear-induced refraction (McWilliams et al. 2004; Kenyon and Sheres 2006) and related Langmuir circulation. The frontal instabilities shown in Figs. 6a and 6b have scales comparable to the dominant wavelength of the surface waves, further suggesting the possibility that the separation of frontal and surface wave scales may not generally apply.

As the various remote sensing applications continue to evolve toward finer spatial resolutions, for example, ocean color and altimeters, detailed knowledge of the surface wave field and its inhomogeneities due to wave–current interaction will become increasingly important. For both active and passive remote sensing, the finescale structure of the ocean surface is of fundamental importance, and the modulation of this structure will be affected by the wave–current interaction processes described here.

Regarding the characterization of wave breaking with respect to the modulation of the spectrum, the data consistently gave larger correlation coefficients between the whitecap coverage against the normalized saturation. Following a suggestion from an anonymous reviewer, we also tested an anisotropic spectral saturation metric introduced by Ardhuin et al. 2010,[3] which is given by

$$\hat{B}(k,\theta) = \int_{\theta-\Delta_\theta}^{\theta+\Delta_\theta} F(k,\varphi)k^3\cos^2(\theta-\varphi)k\,d\varphi, \qquad (5)$$

where $\Delta_\theta = 80°$. It was found that mean anisotropic saturation $\langle \hat{B}(\overline{\theta}_B)\rangle$ along the mean saturation direction $\overline{\theta}_B$ with

$$\overline{\theta}_B = \frac{\iint F(k)\theta k^3\,dk}{\iint F(k)k^3\,dk}$$

correlated the best with the whitecap coverage. The correlation coefficients obtained are 0.71 and 0.56 for the HiRes and GoM datasets, which are similar to those obtained with the normalized saturation (i.e., 0.80 and 0.54, respectively). But again, the correlation differences are not statistically significant compared to those obtained using the mean saturation $\langle B\rangle$.

5. Conclusions

We have presented a characterization of inhomogeneities of the ocean surface wave field over areas with strong wave–current interactions. This was accomplished with novel airborne observations collected during HiRes near Bodega Bay and an experiment in the Gulf of Mexico. Both datasets showed modulation of the wave height due to wave–current interactions by 30%. The analysis from HiRes observations focused on measurements collected on the edge of an upwelling jet, where strong gradients of wave breaking were found. An area of enhanced breaking was identified at the edge of the jet, overlapping with a submesoscale front. The area of enhanced wave breaking separated two breaking regimes, with little breaking to the west and relatively more breaking to the east over the colder SST. Measurements across the submesoscale front

[3] Corrected without the factor of $c_g(2\pi)^{-1}$.

showed maximum vertical vorticity at the edge of the front and a reduction of the mean winds at 30 m MSL over the areas with larger whitecap coverage, which is consistent with an increase of the drag coefficient due to increased wave breaking. Analysis of the wavenumber spectra across the jet showed that the mean saturation B, directional spreading σ, and normalized saturation $\tilde{B}$ varied substantially across the jet, correlating well with the whitecap coverage.

The measurements in the Gulf of Mexico were collected over the edge of the Loop Current and associated eddies after the passage of a cold front. The wave field showed substantial modulation due to currents, including conditions of opposing waves and currents and a focal area. The measured whitecap coverage correlated well with the spectral moments for wavenumbers larger than the spectral peak.

Statistical analysis of wave crests, wave troughs, and crest lengths per unit area showed agreement with analytical distributions from second-order nonlinear approximations, except over the focal area where significant deviations from second-order nonlinear theory were found. Similarly, measured wave height distributions were generally bounded by the generalized Boccotti distribution except over the focal area where the wave height distribution reached the Rayleigh distribution, with $H_{\max} = 2.55H_s$, which is much larger than $2H_s$, the typical threshold criterion used to define extreme waves. However, the measured statistics of extreme wave elevations were bounded by analytical, second-order, nonlinear distributions of spatial extremes.

Finally, it is important to appreciate that surface wave measurements having the accuracy and spatiotemporal coverage displayed here would not have been possible without the advantages of airborne measurements, first, to find regions of strong wave–current interaction and, second, to be able to measure the wave fields over large areas with the accuracy described here.

Acknowledgments. We thank Bill Krabill and NASA for the loan of the ATM lidar and the ATM operator team, James Yungel, Matt Linkswiler, and Earl Frederick during HiRes. We thank the pilots and scientific staff at CIRPAS, especially Haf Jonsson, for making the HiRes Twin Otter flights successful. We are thankful to pilot Bradley Busch, Rick Throckmorton and staff at Aspen Helicopters. We thank Nick Statom for operating the MASS in the Gulf of Mexico. We are thankful to Eric Terrill, Sung Yong Kim, and John Largier for making the HF radar current data available for this work. This work was supported by grants from ONR (N00014-08-1-0499 and N00014-14-1-0710, PI: WKM; N00014-16-1-2936, PI: LR) and NSF (OCE1634289, PI: WKM) and industry (PI: WKM). We thank anonymous reviewers whose comments helped improve the manuscript.

APPENDIX

Wave Parameters

Following Fedele (2012) and Fedele et al. (2013), the number of waves in an area L_xL_y is given by $N_s = \sqrt{2\pi}[(L_xL_y)/(\overline{\lambda}_x\overline{\lambda}_y)]\sqrt{1-\alpha^2}$, where L_x, L_y are the length and width of the wave record, the corresponding mean wavelengths $\overline{\lambda}_x = 2\pi\sqrt{m_{00}/m_{20}}$, $\overline{\lambda}_y = 2\pi\sqrt{m_{00}/m_{02}}$, and $\alpha = m_{11}/\sqrt{m_{02}m_{20}}$. The moments of the directional spectrum are given by $m_{ij} = \iint k_x^i k_y^j F(k)\,dk$. Although the steepness parameter μ is often defined as the product of $\eta_{\text{rms}}k_p$ (e.g., Mori and Janssen 2006; Romero and Melville 2011), for consistency with Fedele et al. (2013), here μ is defined from moments of the frequency spectrum according to $\mu = [(\eta_{\text{rms}}\overline{\omega}^2)/g](1-\nu+\nu^2)$, where $\overline{\omega} = m_1/m_0$ is the spectrally weighted mean frequency and $\nu = \sqrt{m_0m_2/m_1^2 - 1}$ is a measure of the spectral bandwidth. The frequency spectrum $\Psi(\omega) = \phi(k)\partial k/\partial\omega$, with $\omega = (gk)^{1/2}$ according to the linear dispersion relationship, and the moments $m_i = \int \omega^i \psi(\omega)\,d\omega$.

REFERENCES

Alkhalidi, M. A., and M. A. Tayfun, 2013: Generalized Boccotti distribution for nonlinear wave heights. *Ocean Eng.*, **74**, 101–106, doi:10.1016/j.oceaneng.2013.09.014.

Ardhuin, F., and Coauthors, 2010: Semiempirical dissipation source functions for ocean waves. Part I: Definition, calibration, and validation. *J. Phys. Oceanogr.*, **40**, 1917–1941, doi:10.1175/2010JPO4324.1.

——, and Coauthors, 2012: Numerical wave modeling in conditions with strong currents: Dissipation, refraction, and relative wind. *J. Phys. Oceanogr.*, **42**, 2101–2120, doi:10.1175/JPO-D-11-0220.1.

Banner, M. L., and W. L. Peirson, 2007: Wave breaking onset and strength for two-dimensional deep-water wave groups. *J. Fluid Mech.*, **585**, 93–115, doi:10.1017/S0022112007006568.

——, and R. P. Morison, 2010: Refined source terms in wind wave models with explicit wave breaking prediction. Part I: Model framework and validation against field data. *Ocean Modell.*, **33**, 177–189, doi:10.1016/j.ocemod.2010.01.002.

——, J. R. Gemmrich, and D. M. Farmer, 2002: Multiscale measurements of ocean wave breaking probability. *J. Phys. Oceanogr.*, **32**, 3364–3375, doi:10.1175/1520-0485(2002)032<3364:MMOOWB>2.0.CO;2.

——, X. Barthelemy, F. Francesco, M. Allis, A. Benetazzo, F. Dias, and W. L. Peirson, 2014: Linking reduced breaking crest speeds to unsteady nonlinear water wave group behavior. *Phys. Rev. Lett.*, **112**, 114502, doi:10.1103/PhysRevLett.112.114502.

Barbariol, F., A. Benetazzo, S. Carniel, and M. Sclavo, 2015: Space–time wave extremes: The role of Metocean forcings. *J. Phys. Oceanogr.*, **45**, 1897–1916, doi:10.1175/JPO-D-14-0232.1.

Benetazzo, A., F. Barbariol, F. Bergamasco, A. Torsello, S. Carniel, and M. Sclavo, 2015: Observation of extreme sea waves in a space–time ensemble. *J. Phys. Oceanogr.*, **45**, 2261–2275, doi:10.1175/JPO-D-15-0017.1.

Bretherton, F. P., R. E. Davis, and C. B. Fandry, 1976: A technique for objective analysis and design of oceanographic experiments applied to MODE-73. *Deep-Sea Res. Oceanogr. Abstr.*, **23**, 559–582, doi:10.1016/0011-7471(76)90001-2.

Chelton, D. B., M. H. Freilich, J. M. Sienkiewicz, and J. M. Von Ahn, 2006: On the use of QuikSCAT scatterometer measurements of surface winds for marine weather prediction. *Mon. Wea. Rev.*, **134**, 2055–2071, doi:10.1175/MWR3179.1.

Clark, D. B., L. Lenain, F. Feddersen, E. Boss, and R. T. Guza, 2014: Aerial imaging of fluorescent dye in the near shore. *J. Atmos. Oceanic Technol.*, **31**, 1410–1421, doi:10.1175/JTECH-D-13-00230.1.

Davis, R. E., 1985: Objective mapping by least squares fitting. *J. Geophys. Res.*, **90**, 4773–4777, doi:10.1029/JC090iC03p04773.

Denman, K. L., and H. J. Freeland, 1985: Correlation scales, objective mapping and a statistical test of geostrophy over the continental shelf. *J. Mar. Res.*, **43**, 517–539, doi:10.1357/002224085788440402.

Dysthe, K., 2001: Refraction of gravity waves by weak current gradients. *J. Fluid Mech.*, **442**, 157–159, doi:10.1017/S0022112001005237.

——, H. E. Krogstad, and P. Müller, 2008: Oceanic rogue waves. *Annu. Rev. Fluid Mech.*, **40**, 287–310, doi:10.1146/annurev.fluid.40.111406.102203.

Farmer, D. M., C. L. McNeil, and B. D. Johnson, 1993: Evidence for the importance of bubbles in increasing air–sea gas flux. *Nature*, **361**, 620–623, doi:10.1038/361620a0.

Fedele, F., 2012: Space–time extremes in short-crested storm seas. *J. Phys. Oceanogr.*, **42**, 1601–1615, doi:10.1175/JPO-D-11-0179.1.

——, A. Benetazzo, G. Gallego, P. C. Shih, A. Yezzi, F. Barbariol, and F. Ardhuin, 2013: Space–time measurements of oceanic sea states. *Ocean Modell.*, **70**, 103–115, doi:10.1016/j.ocemod.2013.01.001.

Friehe, C. A., and Coauthors, 1991: Air-sea fluxes and surface layer turbulence around a sea surface temperature front. *J. Geophys. Res.*, **96**, 8593–8609, doi:10.1029/90JC02062.

Gallet, B., and W. R. Young, 2014: Refraction of swell by surface currents. *J. Mar. Res.*, **72**, 105–126, doi:10.1357/002224014813758959.

Gordon, H. R., 1997: Atmospheric correction of ocean color imagery in the Earth Observing System era. *J. Geophys. Res.*, **102**, 17 081–17 106, doi:10.1029/96JD02443.

Grare, L., L. Lenain, and W. K. Melville, 2013: Wave-coherent airflow and critical layers over ocean waves. *J. Phys. Oceanogr.*, **43**, 2156–2172, doi:10.1175/JPO-D-13-056.1.

Haus, B. K., 2007: Surface current effects on the fetch-limited growth of wave energy. *J. Geophys. Res.*, **112**, C03003, doi:10.1029/2006JC003924.

Henry, W., 1979: Aspects of the fate of cold fronts in the Gulf of Mexico. *Mon. Wea. Rev.*, **107**, 1078–1082, doi:10.1175/1520-0493(1979)107<1078:SAOTFO>2.0.CO;2.

Huang, Z.-C., B. D. Reineman, L. Lenain, W. K. Melville, and J. H. Middleton, 2012: Airborne lidar measurements of wave energy dissipation in a coral reef lagoon system. *J. Geophys. Res.*, **117**, C03016, doi:10.1029/2011JC007203.

Hwang, P. A., 2005: Altimeter measurements of wind and wave modulation by the Kuroshio in the Yellow and East China Seas. *J. Oceanogr.*, **61**, 987–993, doi:10.1007/s10872-006-0015-0.

——, D. W. Wang, E. J. Walsh, W. B. Krabill, and R. N. Swift, 2000a: Airborne measurements of the wavenumber spectra of ocean surface waves. Part I: Spectral slope and dimensionless spectral coefficient. *J. Phys. Oceanogr.*, **30**, 2753–2767, doi:10.1175/1520-0485(2001)031<2753:AMOTWS>2.0.CO;2.

——, ——, ——, ——, and ——, 2000b: Airborne measurements of the wavenumber spectra of ocean surface waves. Part II: Directional distribution. *J. Phys. Oceanogr.*, **30**, 2768–2787, doi:10.1175/1520-0485(2001)031<2768:AMOTWS>2.0.CO;2.

Janssen, T., and T. Herbers, 2009: Nonlinear wave statistics in a focal zone. *J. Phys. Oceanogr.*, **39**, 1948–1964, doi:10.1175/2009JPO4124.1.

Jury, M. R., 1994: A thermal front within the marine atmospheric boundary layer over the Agulhas Current south of Africa: Composite aircraft observations. *J. Geophys. Res. Oceans*, **99**, 3297–3304, doi:10.1029/93JC02400.

Kaplan, D. M., and J. Largier, 2006: HF radar-derived origin and destination of surface waters off Bodega Bay, California. *Deep-Sea Res. II*, **53**, 2906–2930, doi:10.1016/j.dsr2.2006.07.012.

——, ——, and L. W. Botsford, 2005: HF radar observations of surface circulation off Bodega Bay (Northern California, USA). *J. Geophys. Res.*, **110**, 1–25, doi:10.1029/2005JC002959.

Kenyon, K. E., 1971: Wave refraction in ocean currents. *Deep-Sea Res. Oceanogr. Abstr.*, **18**, 1023–1034, doi:10.1016/0011-7471(71)90006-4.

——, and D. Sheres, 2006: Wave force on an ocean current. *J. Phys. Oceanogr.*, **36**, 212–221, doi:10.1175/JPO2844.1.

Kleiss, J. M., and W. K. Melville, 2010: Observations of wave breaking kinematics in fetch-limited seas. *J. Phys. Oceanogr.*, **40**, 2575–2604, doi:10.1175/2010JPO4383.1.

——, and ——, 2011: The analysis of sea surface imagery for whitecap kinematics. *J. Atmos. Oceanic Technol.*, **28**, 219–243, doi:10.1175/2010JTECHO744.1.

Krabill, W., and C. Martin, 1987: Aircraft positioning using global positioning system carrier phase data. *J. Inst. Navig.*, **34**, 1–21, doi:10.1002/j.2161-4296.1987.tb01487.x.

Kudryavtsev, V. N., S. A. Grodsky, V. A. Dulov, and A. N. Bol'shakov, 1995: Observations of wind waves in the Gulf Stream frontal zone. *J. Geophys. Res.*, **100**, 20 715–20 727, doi:10.1029/95JC00425.

——, D. Akimov, J. Johannessen, and B. Chapron, 2005: On radar imaging of current features: 1. Model and comparison with observations. *J. Geophys. Res.*, **110**, C07016, doi:10.1029/2004JC002505.

Lenain, L., and W. K. Melville, 2017: Evidence of sea-state dependence of aerosol concentration in the marine atmospheric boundary layer. *J. Phys. Oceanogr.*, **47**, 69–84, doi:10.1175/JPO-D-16-0058.1.

Loewen, M., 2002: Inside whitecaps. *Nature*, **418**, 830, doi:10.1038/418830a.

Longuet-Higgins, M. S., 1957: The statistical analysis of a random, moving surface. *Philos. Trans. Roy. Soc. London*, **A249**, 321–387, doi:10.1098/rsta.1957.0002.

Masson, D., 1996: A case study of wave–current interaction in a strong tidal current. *J. Phys. Oceanogr.*, **26**, 359–372, doi:10.1175/1520-0485(1996)026<0359:ACSOWI>2.0.CO;2.

Mathiesen, M., 1987: Wave refraction by a current whirl. *J. Geophys. Res.*, **92**, 3905–3912, doi:10.1029/JC092iC04p03905.

McWilliams, J. C., 2016: Submesoscale currents in the ocean. *Proc. Roy. Soc.*, **A472**, 20160117, doi:10.1098/rspa.2016.0117.

——, J. M. Restrepo, and E. M. Lane, 2004: An asymptotic theory for the interaction of waves and currents in coastal waters. *J. Fluid Mech.*, **511**, 135–178, doi:10.1017/S0022112004009358.

——, J. Gula, M. J. Molemaker, L. Renault, and A. F. Shchepetkin, 2015: Filament frontogenesis by boundary layer turbulence. *J. Phys. Oceanogr.*, **45**, 1988–2005, doi:10.1175/JPO-D-14-0211.1.

Melville, W. K., L. Romero, and J. M. Kleiss, 2005: Extreme wave events in the Gulf of Tehuantepec. *Rogue Waves: Proc. 14th*

'Aha Huliko'a Hawaiian Winter Workshop, University of Hawai'i at Mānoa, Honolulu, Hawaii, 23–28.

——, L. Lenain, D. R. Cayan, M. Kahru, J. P. Kleissl, P. Linden, and N. M. Statom, 2016: The Modular Aerial Sensing System. *J. Atmos. Oceanic Technol.*, **33**, 1169–1184, doi:10.1175/JTECH-D-15-0067.1.

Moore, K. D., K. J. Voss, and H. R. Gordon, 2000: Spectral reflectance of whitecaps: Their contribution to water-leaving radiance. *J. Geophys. Res.*, **105**, 6493–6499, doi:10.1029/1999JC900334.

Mori, N., and P. A. E. M. Janssen, 2006: On kurtosis and occurrence probability of freak waves. *J. Phys. Oceanogr.*, **36**, 1471–1483, doi:10.1175/JPO2922.1.

Munk, W. H., G. R. Miller, F. E. Snodgrass, and N. F. Barber, 1963: Directional recording of swell from distant storms. *Philos. Trans. Roy. Soc. London*, **A255**, 505–584, doi:10.1098/rsta.1963.0011.

——, L. Armi, K. Fischer, and F. Zachariasen, 2000: Spirals on the sea. *Proc. Roy. Soc. London*, **A456**, 1217–1280, doi:10.1098/rspa.2000.0560.

——, G. R. Miller, F. E. Snodgrass, and N. F. Barber, 2013: Correction: Directional recording of swell from distant storms. *Philos. Trans. Roy. Soc. London*, **A371**, 20130039, doi:10.1098/rsta.2013.0039.

Onorato, M., D. Proment, and A. Toffoli, 2011: Triggering rogue waves in opposing currents. *Phys. Rev. Lett.*, **107**, 184502, doi:10.1103/PhysRevLett.107.184502.

Pearman, D. W., T. H. C. Herbers, T. T. Janssen, H. D. van Ettinger, S. A. McIntyre, and P. F. Jessen, 2014: Drifter observations of the effects of shoals and tidal-currents on wave evolution in San Francisco Bight. *Cont. Shelf Res.*, **91**, 109–119, doi:10.1016/j.csr.2014.08.011.

Phillips, O. M., 1977: *The Dynamics of the Upper Ocean*. Cambridge University Press, 344 pp.

——, 1984: On the response of short ocean wave components at a fixed wavenumber to ocean current variations. *J. Phys. Oceanogr.*, **14**, 1425–1433, doi:10.1175/1520-0485(1984)014<1425:OTROSO>2.0.CO;2.

——, 1985: Spectral and statistical properties of the equilibrium range in wind-generated gravity waves. *J. Fluid Mech.*, **156**, 505–531, doi:10.1017/S0022112085002221.

Pizzo, N. E., and W. K. Melville, 2016: Wave modulation: The geometry, kinematics, and dynamics of surface-wave focusing. *J. Fluid Mech.*, **803**, 292–312, doi:10.1017/jfm.2016.473.

Plant, W. J., W. C. Keller, and K. Hayes, 2005: Simultaneous measurement of ocean winds and waves with an airborne coherent real aperture radar. *J. Atmos. Oceanic Technol.*, **22**, 832–846, doi:10.1175/JTECH1724.1.

Rapp, R. J., and W. K. Melville, 1990: Laboratory measurements of deep-water breaking waves. *Philos. Trans. Roy. Soc. London*, **A331**, 735–800, doi:10.1098/rsta.1990.0098.

Reineman, B. D., L. Lenain, C. David, and W. K. Melville, 2009: A portable airborne scanning lidar system for ocean and coastal applications. *J. Atmos. Oceanic Technol.*, **26**, 2626–2641, doi:10.1175/2009JTECHO703.1.

Romero, L., and W. K. Melville, 2010a: Numerical modeling of fetch-limited waves in the Gulf of Tehuantepec. *J. Phys. Oceanogr.*, **40**, 466–468, doi:10.1175/2009JPO4128.1.

——, and ——, 2010b: Airborne observations of fetch-limited waves in the Gulf of Tehuantepec. *J. Phys. Oceanogr.*, **40**, 441–465, doi:10.1175/2009JPO4127.1.

——, and ——, 2011: Spatial statistics of the sea surface in fetch-limited conditions. *J. Phys. Oceanogr.*, **41**, 1821–1841, doi:10.1175/2011JPO4535.1.

——, ——, and J. M. Kleiss, 2012: Spectral energy dissipation due to surface-wave breaking. *J. Phys. Oceanogr.*, **42**, 1421–1444, doi:10.1175/JPO-D-11-072.1.

Stansell, P., and C. MacFarlane, 2002: Experimental investigation of wave breaking criteria based on wave phase speeds. *J. Phys. Oceanogr.*, **32**, 1269–1283, doi:10.1175/1520-0485(2002)032<1269:EIOWBC>2.0.CO;2.

Sullivan, P. P., J. C. McWilliams, and E. G. Patton, 2014: Large-eddy simulation of marine atmospheric boundary layers above a spectrum of moving waves. *J. Atmos. Sci.*, **71**, 4001–4027, doi:10.1175/JAS-D-14-0095.1.

Sutherland, P., and W. K. Melville, 2013: Field measurements and scaling of ocean surface wave-breaking statistics. *Geophys. Res. Lett.*, **40**, 3074–3079, doi:10.1002/grl.50584.

——, and ——, 2015: Field measurements of surface and near-surface turbulence in the presence of breaking waves. *J. Phys. Oceanogr.*, **45**, 943–965, doi:10.1175/JPO-D-14-0133.1.

Tayfun, M. A., 1980: Narrow-band nonlinear sea waves. *J. Geophys. Res.*, **85**, 1548–1552, doi:10.1029/JC085iC03p01548.

Thorpe, S. A., 1982: On the clouds of bubbles formed by breaking wind-waves in deep water, and their role in air-sea gas transfer. *Philos. Trans. Roy. Soc. London*, **A304**, 155–210, doi:10.1098/rsta.1982.0011.

Toffoli, A., E. Bitner-Gregersen, M. Onorato, and A. V. Babanin, 2008: Wave crest and trough distributions in a broad-banded directional wave field. *Ocean Eng.*, **35**, 1784–1792, doi:10.1016/j.oceaneng.2008.08.010.

——, T. Waseda, H. Houtani, L. Cavaleri, D. Greaves, and M. Onorato, 2015: Rogue waves in opposing currents: An experimental study on deterministic and stochastic wave trains. *J. Fluid Mech.*, **769**, 277–297, doi:10.1017/jfm.2015.132.

Vincent, C. E., 1979: The interaction of wind-generated sea waves with tidal currents. *J. Phys. Oceanogr.*, **9**, 748–755, doi:10.1175/1520-0485(1979)009<0748:TIOWGS>2.0.CO;2.

Wang, D. W., A. K. Liu, C. Y. Peng, and E. A. Meindl, 1994: Wave-current interaction near the Gulf Stream during the surface wave dynamics experiment. *J. Geophys. Res.*, **99**, 5065–5079, doi:10.1029/93JC02714.

White, B., and B. Fornberg, 1998: On the chance of freak waves at sea. *J. Fluid Mech.*, **355**, 113–138, doi:10.1017/S0022112097007751.